CCFE-PR(16)67

D. Moulton, J. Harrison, B. Lipschultz, and D. Coster

Using SOLPS to confirm the importance of parallel area expansion in Super-X divertors

Using SOLPS to confirm the importance of parallel area expansion in Super-X divertors

D. Moulton[1], J. Harrison[1], B. Lipschultz[2], and D. Coster[3]

[1]Culham Centre for Fusion Energy, Culham Science Centre, Abingdon, OX14 3DB, UK
[2]Department of Physics, University of York, Heslington, York, YO10 5DD, UK
[3]Max-Planck Institut für Plasmaphysik, Boltzmannstraße 2, D-85748 Garching, Germany

Using SOLPS to confirm the importance of parallel area expansion in Super-X divertors

D. Moulton[1], J. Harrison[1], B. Lipschultz[2], D. Coster[3]

1 Culham Centre for Fusion Energy, Culham Science Centre, Abingdon, OX14 3DB, UK

2 Department of Physics, University of York, Heslington, York, YO10 5DD, UK

3 Max-Planck Institut für Plasmaphysik, Boltzmannstraße 2, D-85748 Garching, Germany

E-mail: david.moulton@ukaea.uk

August 2016

Abstract. We show that a central characteristic of Super-X divertors, parallel area expansion f_R (defined as the ratio of the elementary area normal to the magnetic field at the target to that at the X-point, also known as total flux expansion), significantly changes the characteristics of the target plasma for fixed upstream conditions. To isolate the effect of parallel area expansion from other effects, we utilise SOLPS-5.0 simulations of an isolated slot divertor leg in a minimally complex, rectangular geometry. The grid is rotated outwards about the X-point in order to perform a scan in which only the parallel area expansion changes. We find that if the SOL remains in the attached, conduction-limited regime throughout the scan, the target electron density (temperature) scales approximately as f_R^2 ($1/f_R^2$), in good agreement with the modified two-point model presented in (Petrie T W *et al* 2013 *Nucl. Fusion* **53** 113024). If, however, the SOL transitions from the sheath-limited regime to the conduction-limited regime during the scan, the simulated scalings of target electron temperature and density are weaker than predicted by the modified two-point model. The upstream density for transition from sheath- to conduction-limited regimes is found to scale approximately with $1/f_R$, in agreement with the modified two-point model. Assessing upstream-density-driven detachment onset, we find that the target electron temperature at which target density rollover occurs (~ 0.6 eV) is independent of f_R. Given this, the modified two-point model predicts a halving of the upstream (and target) densities at which rollover occurs when f_R is doubled, in good agreement with the simulation results.

1. Introduction

The Super-X divertor has been proposed as a means to reduce the large plasma energy flux densities and physical sputtering at the targets of fusion reactors (Kotschenreuther *et al* 2010). There are two defining aspects of a Super-X divertor which distinguish it from a conventional divertor: (i) increased major radius at the target relative to the X-point (this leads to an increased parallel area expansion from X-point to target, which in

turn leads to a reduced parallel energy flux density at the target‡); (ii) increased parallel and poloidal distances from X-point to target. In addition, the Super-X divertor of the forthcoming MAST-Upgrade machine (Fishpool *et al* 2013) will use a baffle around the divertor entrance to increase the neutral compression relative to conventional divertors.

In this contribution, we isolate and study the effect of increased parallel area expansion. From conservation of magnetic flux we have that $dA_{\|t}B_t = dA_{\|u}B_u$, where $dA_\|$ is the elementary area normal to the total magnetic field B and subscripts t and u denote target and X-point ('u' for 'upstream') quantities, respectively. We define the parallel area expansion as $f_R \equiv dA_{\|t}/dA_{\|u} = B_u/B_t \approx R_t/R_u$§, where R is the major radius. In the model used here, the ratio of poloidal and toroidal magnetic field components is kept constant so that the latter approximation is, in fact, exact.

Several authors have addressed the effect of parallel area expansion on attached divertor conditions using variations of the two-point model (Petrie *et al* 2013, Kotschenreuther *et al* 2010, Stangeby *et al* 2000). (Petrie *et al* 2013) predicted that in the attached, conduction-limited phase, the target electron density and temperature scale approximately with f_R^2 and $1/f_R^2$, respectively. (Lipschultz *et al* 2016), using a model based on energy balance, predicted that the upstream density required for detachment onset scales with $1/f_R$, while the upstream density required for the thermal front to reach the X-point is independent of f_R (i.e. the detachment 'window' increases with f_R, making detachment control easier). If shown to be true, such strong effects would greatly benefit the Super-X divertor over the conventional divertor, by decreasing the physical sputtering yield (for the same upstream collisionality), lowering the upstream collisionality at which detachment onset occurs, and making detachment easier to control. This could potentially bring closer the ultimate goal of a detached target plasma that is compatible with a steady-state, reactor-relevant, low-collisionality core plasma with self-sustained current drive.

In *realistic* geometries, however, experimental and modelling analyses are more mixed in their support of parallel area expansion. (Havlíčková *et al* 2015) showed that, for the same upstream conditions, the MAST-Upgrade Super-X divertor leads to a higher density, lower temperature target plasma than a conventional divertor. That difference meant that the Super-X also detached at lower upstream density. (Umansky *et al* 2016), in contrast, reported that their UEDGE modelling of several different divertor configurations show little effect of the target major radius on the detachment input power threshold. (Theiler *et al* 2016) reported that, in TCV experiments, the line-averaged electron density at which the target ion flux rolls over is indistinguishable when the target major radius is increased by a factor 1.3. (Petrie *et al* 2013) showed

‡ This also results in a reduced energy flux density *felt* by the target if, by decreasing the poloidal magnetic field at the target, the angle between the target plate and the total magnetic field is kept constant as the strike point major radius is increased.

§ This quantity has been previously referred to as 'total flux expansion', e.g. (Lipschultz *et al* 2016, Theiler *et al* 2016). Here we choose the nomenclature 'parallel area expansion', since it is the parallel area that is changing while the magnetic flux is conserved.

that the target electron density and temperature depend only weakly on target major radius in DIII-D. The authors proposed that this was due to changes in the neutral pathways as the target was swept out; the higher target major radius configuration also had a more open divertor, potentially attenuating the effect of increased parallel area expansion.

In all of these realistic geometry studies (both experimental and modelling), it is impossible to eliminate confounding variables when scanning the parallel area expansion. These can include (but are not limited to) the neutral pathways, radial transport in the divertor, SOL width at the divertor entrance, pitch angle, impurity content, parallel and poloidal distances from X-point to target – all of which can change when the target major radius is moved in a real tokamak. The role of parallel area expansion alone is therefore difficult to assess. On the other hand, two-point models like the one presented by (Petrie *et al* 2013) ignore physics which may, in reality, be important (e.g. neutral physics, radial transport, viscosity, unequal electron and ion temperatures, non-unity target Mach numbers and the transition from sheath- to conduction-limited regimes).

In this study, we attempt to bridge the gap between models with simplified physics and simplified geometry, and models (or experiments) with realistic physics and realistic geometry, by assessing a model with 'realistic' physics (or at least with a lot of the physics ignored by (Petrie *et al* 2013)) in a simplified geometry. This model utilises SOLPS-5.0 in an isolated, rectangular, slot divertor leg. By rotating the leg about the X-point, a scan is performed in which the only parameter that changes is the parallel area expansion. The scalings of the target plasma in the face of the additional physics of SOLPS-5.0 are then compared to those of (Petrie *et al* 2013). Furthermore, we perform upstream density scans for the two extremes of our parallel area expansion scan, in order to assess the effect of parallel area expansion on the transition from sheath- to conduction-limited regimes and on detachment onset.

2. Simulation setup

2.1. Grids

In order to isolate the effect of varying parallel area expansion, SOLPS-5.0 simulations were run on grids with a minimally complex, rectangular geometry, which spanned a single isolated divertor leg. By rotating these grids about the X-point and fixing the boundary conditions at the upstream divertor entrance (section 2.3), a clean scan was obtained, in which only the parallel area expansion changed.

The simulation geometry is shown in figure 1, with poloidal, radial and toroidal directions labelled x, y and z, respectively, and with vertical and major radius coordinates labelled Z and R. Note that although rectangular in the poloidal plane, this is not a slab geometry; the toroidal direction is truly toroidal. The B2.5 (plasma fluid) grid was of size $n_x = 200$ by $n_y = 40$. Cells were spaced evenly in the radial direction (with $dy = 6$ mm everywhere) and squeezed poloidally towards the target (with $dx = 1.5$

mm at the target). The EIRENE walls coincided with the edges of the B2.5 grid. The grid dimensions and magnetic field were chosen to be similar to MAST-U values, as follows. The poloidal distance from the X-point (positioned at $R = 1$ m, $Z = 0$) to the target was 1 m and the radial distance across the grid was 0.25 m. For the toroidal magnetic field we made a MAST-U-like assumption that $B_z = \alpha_z/R$ (with $\alpha_z = 0.5$ Tm), while for the poloidal magnetic field, given by $B_x = \alpha_x/R$ (with $\alpha_x = 0.025$ Tm), we also chose to have a $1/R$ dependence so as to conserve poloidal flux on the orthogonal grid. The resulting parallel connection length from X-point to target was $L = 20$ m.

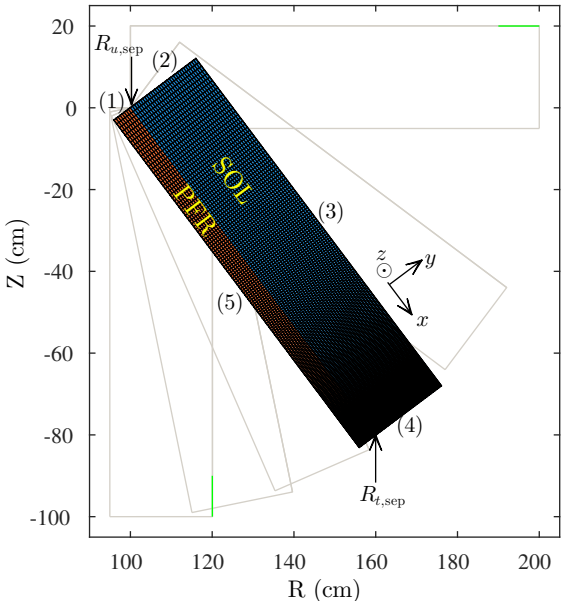

Figure 1. Minimally complex, isolated divertor leg grid for the $f_R = 1.6$ case. Other grids, outlined in grey, were created by rotation about the X-point, keeping poloidal flux expansion fixed at unity and the parallel connection length fixed at $L = 20$ m. The boundary conditions for surfaces (1)-(5) are given in section 2.3. The toroidally symmetric pumping surfaces used for the density ramps to detachment, described in section 4, are shown in green. Colour version available online.

The highlighted grid in figure 1 is for the particular $f_{R,\mathrm{sep}} = R_{t,\mathrm{sep}}/R_{u,\mathrm{sep}} = 1.6$ case (henceforth we drop the 'sep' notation from f_R since we only analyse flux rings near the separatrix, for which $f_R \approx f_{R,\mathrm{sep}}$ to within 1%). A regularly spaced six-point scan in f_R from $f_R = 1$ to $f_R = 2$ was carried out by rotating the grid about the fixed X-point, resulting in the other grids used in this study (outlined in grey) in figure 1.

The deliberate simplification of the geometry outlined above ensured that the poloidal flux expansion (fixed at unity), connection length, target angle to the poloidally projected magnetic field, pitch angle and neutral geometry all remained constant across all of the grids used here. Variation in these confounding variables would have been unavoidable in a scan over f_R using more realistic geometries, making interpretation of the results more difficult. The only relevant quantity that changes in our simplified f_R scan is f_R itself.

2.2. Equations

In the absence of currents, drifts and impurities and with the particular (simplifying) code input parameters chosen for these simulations, the plasma equations solved here are as follows (see also Schneider *et al* 2006 and Dekeyser *et al* 2011). Particle conservation is given by

$$\frac{\partial n}{\partial t}+\frac{1}{\sqrt{g}}\frac{\partial}{\partial x}\left(\frac{\sqrt{g}}{h_x}nu_x\right)+\frac{1}{\sqrt{g}}\frac{\partial}{\partial y}\left(\frac{\sqrt{g}}{h_y}nu_y\right)=S^{\text{neut}}_{\text{part}}, \tag{1}$$

where $n=n_e=n_i$ is the pure deuterium plasma density, $u_x=b_xu_\parallel$ is the poloidal projection of the parallel plasma velocity $u_\parallel$, $b_x=B_x/B$ is the sine of the pitch angle, $u_y=-\frac{D^n}{n}\frac{1}{h_y}\frac{\partial n}{\partial y}$ is the radial plasma velocity, D^n_y is the prescribed anomalous radial particle diffusivity, $S^{\text{neut}}_{\text{part}}$ is the particle source due to neutrals, $h_x=1/||\nabla x||$, $h_y=1/||\nabla y||$, $\sqrt{g}=h_xh_yh_z$ and $h_z=2\pi R$ are the metric coefficients. Conservation of parallel momentum is given by

$$\begin{aligned}\frac{\partial}{\partial t}\left(mnu_\parallel\right)+\frac{1}{\sqrt{g}}\frac{\partial}{\partial x}\left(\frac{\sqrt{g}}{h_x}mnu_xu_\parallel-\frac{\sqrt{g}}{h_x^2}\frac{4}{3}b_x\eta^i_\parallel\frac{\partial u_\parallel}{\partial x}\right)\\ +\frac{1}{\sqrt{g}}\frac{\partial}{\partial y}\left(\frac{\sqrt{g}}{h_y}mnu_yu_\parallel-\frac{\sqrt{g}}{h_y^2}\eta^i_y\frac{\partial u_\parallel}{\partial y}\right)=-\frac{b_x}{h_x}\frac{\partial p}{\partial x}+S^{\text{neut}}_{\text{mom}},\end{aligned} \tag{2}$$

where m is the deuterium ion mass, $\eta^i_\parallel$ is the Balescu parallel ion viscosity (Balescu 1988), $\eta^i_y=mnD^n_y$ is the radial viscosity, $p=n(T_e+T_i)$ is the static pressure, T_e is the electron temperature, T_i is the ion temperature and $S^{\text{neut}}_{\text{mom}}$ is the parallel momentum source due to neutrals. The internal electron energy equation is given by

$$\begin{aligned}\frac{\partial}{\partial t}\left(\frac{3}{2}nT_e\right)+\frac{1}{\sqrt{g}}\frac{\partial}{\partial x}\left(\sqrt{g}h_x\tilde{q}_{ex}\right)+\frac{1}{\sqrt{g}}\frac{\partial}{\partial y}\left(\frac{\sqrt{g}}{h_y}\tilde{q}_{ey}\right)=-\frac{nT_e}{\sqrt{g}}\frac{\partial}{\partial x}\left(\frac{\sqrt{g}}{h_x}u_x\right)\\ -k_{eq}\left(T_e-T_i\right)+S^{\text{neut}}_{\text{eIE}},\end{aligned} \tag{3}$$

where $\tilde{q}_{ex}=\frac{3}{2}nu_xT_e-\frac{1}{h_x}\kappa^e_x\frac{\partial T_e}{\partial x}$ is the poloidal electron internal energy flux density, κ^e_x is the Balescu electron heat conductivity (Balescu 1988), $\tilde{q}_{ey}=\frac{5}{2}nu_yT_e-\frac{1}{h_y}n\chi^e_y\frac{\partial T_e}{\partial y}$ is the radial electron internal energy flux density, χ^e_y is the prescribed anomalous radial electron heat diffusivity, k_{eq} is the equilibration coefficient (Dekeyser *et al* 2011) and $S^{\text{neut}}_{\text{eIE}}$ is the electron internal energy source due to neutrals. Finally, the ion internal energy equation is given by

$$\begin{aligned}\frac{\partial}{\partial t}\left(\frac{3}{2}nT_i\right)+\frac{1}{\sqrt{g}}\frac{\partial}{\partial x}\left(\frac{\sqrt{g}}{h_x}\tilde{q}_{ix}\right)+\frac{1}{\sqrt{g}}\frac{\partial}{\partial y}\left(\frac{\sqrt{g}}{h_y}\tilde{q}_{iy}\right)=-\frac{nT_i}{\sqrt{g}}\frac{\partial}{\partial x}\left(\frac{\sqrt{g}}{h_x}u_x\right)\\ +k_{eq}\left(T_e-T_i\right)+\frac{4}{3}b_x\eta^i_x\left(\frac{1}{h_x}\frac{\partial u_\parallel}{\partial x}\right)^2+\eta^i_y\left(\frac{1}{h_y}\frac{\partial u_\parallel}{\partial y}\right)^2+S^{\text{neut}}_{\text{iIE}},\end{aligned} \tag{4}$$

where $\tilde{q}_{ix}=\frac{3}{2}nu_xT_i-\frac{1}{h_x}\kappa^i_x\frac{\partial T_i}{\partial x}$ is the poloidal ion internal energy flux density, κ^i_x is the Balescu ion heat conductivity (Balescu 1988), $\tilde{q}_{iy}=\frac{5}{2}nu_yT_i-\frac{1}{h_y}n\chi^i_y\frac{\partial T_i}{\partial y}$ is the radial ion internal energy flux density, χ^i_y is the prescribed anomalous radial ion heat diffusivity and $S^{\text{neut}}_{\text{iIE}}$ is the ion internal energy source due to neutrals. The source terms due to neutrals in equations (1)-(4) were calculated by EIRENE (Reiter 2005). All of the

reactions listed in table 1 of (Kotov *et al* 2008) were included. In all that follows, subscript 'u' refers to upstream values at the divertor entrance and subscript 't' refers to values at the target.

2.3. Boundary conditions

The simplified geometry outlined above allows us to specify boundary conditions at the divertor entrance. The upstream radial energy flux density profile that the divertor has to exhaust, as well as the upstream radial density profile, can therefore be kept fixed throughout the scan in f_R (note that ensuring the same divertor entrance profiles across the f_R scan would be very difficult if the divertor leg were not isolated).

The distinction between the private flux region (PFR) and the scrape-off layer (SOL) region, separated by the separatrix at $y = y_{\rm sep}$, was modelled by choosing different boundary conditions on surfaces (1) and (2) of the upstream boundary. These surfaces are labelled in figure 1 and run from $y = y_{\rm sep} - \Delta y_{\rm PFR}$ to $y = y_{\rm sep}$ for the upstream PFR surface (1) and from $y = y_{\rm sep}$ to $y = y_{\rm sep} + \Delta y_{\rm SOL}$ for upstream SOL surface (2), with $\Delta y_{\rm SOL} = 4\Delta y_{\rm PFR} = 20$ cm chosen. On boundary (1) we assumed $u_{xu} = n_u u_{xu} = \tilde{q}_{exu} = \tilde{q}_{ixu} = 0$ to mimic perfectly symmetric inner and outer PFRs with a stagnation point at the X-point. On boundary (2) we assumed $n_u = n_{u,\rm sep} \exp\left(-(y - y_{\rm sep})/\lambda_n\right)$, $\partial u_{xu}/\partial x = 0$ and $\tilde{q}_{exu} = \tilde{q}_{ixu} = \tilde{q}_{u,\rm sep} \exp\left(-(y - y_{\rm sep})/\lambda_q\right)$, with $n_{u,\rm sep}$, λ_n, $P_{\rm in} \equiv \int_{y_{\rm sep}}^{y_{\rm sep}+\Delta y_{\rm SOL}} (\tilde{q}_{exu} + \tilde{q}_{ixu})\, dy$ and λ_q specified as input parameters. Neutrals that reached the upstream boundary (either surface (1) or (2)) were removed from the simulation domain; we assumed that such neutrals were subsequently ionised and transported in the main plasma in such a way as to set up the prescribed upstream plasma boundary conditions.

At the radial walls we assumed a zero radial flux of particles, parallel momentum and internal energy. At the target we set $u_{\|t} \geq c_{st}$ (where c_{st} is the target sound speed), $\tilde{q}_{ext} = \gamma_e n_t u_{xt} T_{et}$ (with $\gamma_e = 4$), $\tilde{q}_{ixt} = \gamma_i n_t u_{xt} T_{it}$ (with $\gamma_i = 3/2$) and assumed an extrapolation boundary condition for n_t. Both ions and neutrals incident on the target were recycled as deuterium molecules with a recycling fraction $F_{\rm recyc}$. To mimic active pumping, a fraction $F_{\rm pump}$ of neutrals incident on the green surfaces shown in figure 1 could also be removed. The simulations were evolved until, in steady state, the convective plasma flux coming in through the divertor entrance (surface (4)) was equal to the total pumped flux.

3. Attached plasmas; results and analysis

3.1. Scaling of target density and temperature with parallel area expansion; comparison to the modified two-point model

The original two-point model (2PM) (Stangeby 2000) was modified in (Petrie *et al* 2013) to account for variations in f_R. This 'modified 2PM' predicts the following analytic

scalings for n_t and T_{et} with f_R:

$$n_t \propto f_R^2 \left[\frac{\ln f_R}{f_R - 1}\right]^{6/7}, \tag{5}$$

$$T_{et} \propto \frac{1}{f_R^2} \left[\frac{\ln f_R}{f_R - 1}\right]^{-4/7}. \tag{6}$$

A range of SOLPS simulations were run to steady-state in order to test the validity of these scalings across a wide range of parameter space. Input parameters were chosen such that the target plasma remained attached across the whole range of f_R for all of the scans presented in this section. For the reference scan over f_R we set $D_y^n = \chi_y^e = \chi_y^i = 1$ $\mathrm{m^2 s^{-1}}$, $\lambda_n = 10$ cm, $\lambda_q = 5$ cm, $n_{u,\mathrm{sep}} = 1 \times 10^{19}$ $\mathrm{m^{-3}}$, $P_{\mathrm{in}} = 2$ MW, $F_{\mathrm{recyc}} = 0.99$ and $F_{\mathrm{pump}} = 0$. These values for λ_n and λ_q are consistent with fall off lengths at the outer mid-plane of MAST (Kirk *et al* 2004, Thornton *et al* 2014), assuming a realistic poloidal flux expansion of ~ 10 from the outer mid-plane to the divertor entrance. From this reference scan, additional scans were run in which: (i) λ_n was decreased to 5 cm, (ii) λ_q was decreased to 1 cm, (iii) $n_{u,\mathrm{sep}}$ was increased to 2×10^{19} $\mathrm{m^{-3}}$, (iv) P_{in} was increased to 4 MW, (v) F_{recyc} was increased to 0.999 (i.e. a factor 10 decrease in the pumping speed).

Figures 2a and 2b show the resulting absolute values of n_t and T_{et} as a function of f_R for all of these scans, demonstrating the range of n_t and T_{et} that was covered. For each scan, we have taken the target values at the position of maximum target internal energy flux density (for different scans this position could vary from the first to the third SOL ring, i.e. between 0.3 and 1.6 cm from the separatrix, but within each scan the position of this maximum did not change). The same data, plotted now as fractional changes relative to the values at $f_R = 1$, are shown in figures 2c and 2d, with the modified 2PM scalings plotted as solid black lines for comparison. For completeness, in Appendix A.1 we also compare how the target parallel energy flux density in the simulations scales with the parallel area expansion.

We find that for the higher density scan, in which $n_{u,\mathrm{sep}}$ was increased from 1×10^{19} $\mathrm{m^{-3}}$ to 2×10^{19} $\mathrm{m^{-3}}$, the modified 2PM scalings for both n_t and T_{et} are almost exactly recovered by SOLPS. For the other scans, however, the SOLPS scalings of n_t and T_{et} with f_R are weaker than those predicted by the modified 2PM. The weakest scaling was obtained for the high power case, in which a doubling of f_R caused n_t (T_{et}) to increase (decrease) by a factor of just 1.35 (0.51), compared to a factor of 2.92 (0.31) predicted by the modified 2PM. The observed discrepancies between the modified 2PM scaling and those calculated by SOLPS will now be analysed in more detail.

3.2. Analysis of deviations from the modified two-point model

In order to understand the discrepancies shown in figure 2 between the modified 2PM scalings and SOLPS, we will use the 'two-point model formulation' equations (Stangeby *et al* 2015, Kotov and Reiter 2009). These give the following *exact* expressions for n_t

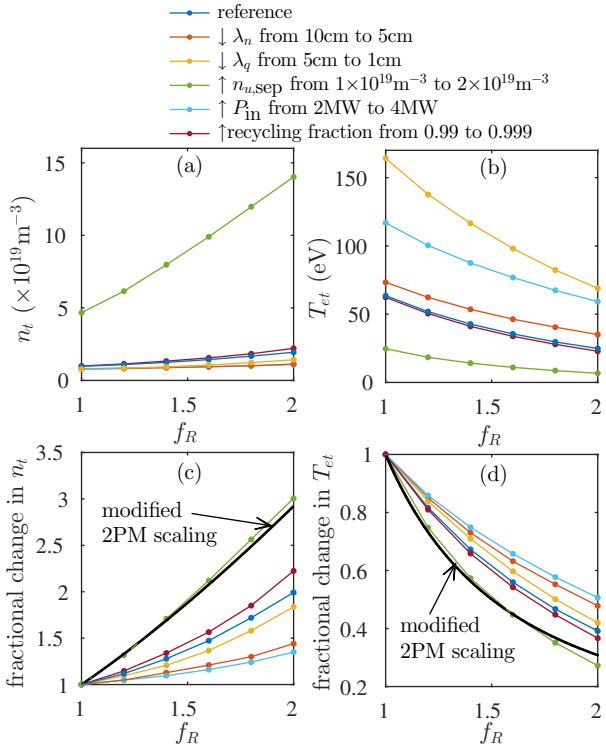

Figure 2. Simulated n_t and T_{et} as a function of f_R for various simulation scans, as labelled. Values are plotted at the position of maximum target internal energy flux density. (a) and (b) show absolute values while (c) and (d) show the fractional changes relative to the $f_R = 1$ case, with the modified two-point model scalings (5) and (6) shown for comparison (black lines). Colour version available online.

and T_{et} at the downstream end of each SOLPS flux ring:

$$n_t = \left[\frac{\gamma^2}{32m}\right]\left[\frac{p_{\mathrm{tot},u}^3}{\tilde{q}_{\parallel u}^2}\right]\left[\frac{(1-f_{\mathrm{momloss}})^3}{(1-f_{\mathrm{pwrloss}})^2}\right]\left[\frac{4}{(1+T_{it}/T_{et})^2}\right]\left[\frac{8M_t^2}{(1+M_t^2)^3}\right]\left[\left(\frac{B_u}{B_t}\right)^2\right], \tag{7}$$

$$T_{et} = \left[\frac{8m}{e\gamma^2}\right]\left[\frac{\tilde{q}_{\parallel u}^2}{p_{\mathrm{tot},u}^2}\right]\left[\frac{(1-f_{\mathrm{pwrloss}})^2}{(1-f_{\mathrm{momloss}})^2}\right]\left[\frac{(1+T_{it}/T_{et})}{2}\right]\left[\frac{(1+M_t^2)^2}{4M_t^2}\right]\left[\left(\frac{B_t}{B_u}\right)^2\right], \tag{8}$$

where $\gamma \equiv (\tilde{q}_{ext} + \tilde{q}_{ixt})/(n_t u_{xt} T_{et}) = \gamma_e + \gamma_i T_{it}/T_{et}$ is the total sheath internal energy transmission coefficient, $p_{\mathrm{tot},u} \equiv p_u + m n_u u_{\parallel u}^2$ is the total (static plus dynamic) upstream pressure, $\tilde{q}_{\parallel u} \equiv (\tilde{q}_{exu} + \tilde{q}_{ixu})/b_x$ is the total (ion plus electron) parallel internal energy flux density entering the top of the considered flux ring, $M_t \equiv \sqrt{m n_t u_{\parallel t}^2/p_t}$ is the target Mach number, $f_{\mathrm{momloss}} = \left(\int_t^u S_{\mathrm{mom}}^{\mathrm{tot}} dl\right)/p_{\mathrm{tot,u}}$ is the fraction of total pressure lost between the upstream end of the flux ring and the target, and $f_{\mathrm{pwrloss}} = \left(\int_t^u S_{\mathrm{IE}}^{\mathrm{tot}} dV\right)/(s_u^y \tilde{q}_{xu})$ is the fraction of internal energy flux lost along the considered flux ring (here, $dl = h_x dx/b_x$ is the line length of a cell in the parallel direction, $dV = \sqrt{g}dxdy$ is the cell volume and $s^y = \left(\sqrt{g}/h_x\right)dy$ is the area seen by poloidal fluxes). The definitions of $S_{\mathrm{mom}}^{\mathrm{tot}}$ and $S_{\mathrm{IE}}^{\mathrm{tot}}$ are given in Appendix A.2.

For the purposes of this analysis it is useful to rewrite equations (7) and (8) as

$$n_t = \left[\frac{1}{32m\tilde{q}_{\parallel u}^2}\right]\left[\frac{4\gamma^2}{(1+T_{it}/T_{et})^2}\right]\left[\frac{p_{\mathrm{tot},u}^3}{[\ln f_R/(f_R-1)]^{6/7}}\right] \left[\frac{(1-f_{\mathrm{momloss}})^3}{(1-f_{\mathrm{pwrloss}})^2}\right]\left[\frac{8M_t^2}{(1+M_t^2)^3}\right] f_R^2 \left[\frac{\ln f_R}{f_R-1}\right]^{6/7}, \tag{9}$$

$$T_{et} = \left[\frac{8m\tilde{q}_{\parallel u}^2}{e}\right]\left[\frac{(1+T_{it}/T_{et})}{2\gamma^2}\right]\left[\frac{[\ln f_R/(f_R-1)]^{4/7}}{p_{\mathrm{tot},u}^2}\right] \left[\frac{(1-f_{\mathrm{pwrloss}})^2}{(1-f_{\mathrm{momloss}})^2}\right]\left[\frac{(1+M_t^2)^2}{4M_t^2}\right]\frac{1}{f_R^2}\left[\frac{\ln f_R}{f_R-1}\right]^{-4/7}. \tag{10}$$

In this form we can see that the first factors in both (9) and (10) are constant across an f_R scan, while the last factors are just the modified 2PM scalings (5) and (6). The 2nd to 5th factors therefore represent the additional physics in this SOLPS-5.0 model which is not present in the modified 2PM. If the product of these 2nd to 5th factors varies as a function of f_R then the simulations will deviate from the modified 2PM scaling. If, however, the assumptions used by (Petrie *et al* 2013) when deriving the modified 2PM are well met (i.e. that $f_{\mathrm{momloss}} = f_{\mathrm{pwrloss}} = 0$, $T_e = T_i$, $M_t = 1$, $p_{\mathrm{tot},u} = p_u$ and $T_{eu} \propto [\ln f_R/(f_R-1)]^{2/7}$ ‡), then the 2nd to 5th factors will not vary with f_R and SOLPS-5.0 will recover the modified 2PM scaling.

In figure 3 we plot the fractional change, from $f_R = 1$ to $f_R = 2$ (i.e. across the extremes of the f_R scan), in the 2nd to 5th factors of equation (9) (figure 3a, explaining n_t discrepancies) and equation (10) (figure 3b, explaining T_{et} discrepancies). The fractional change in each factor is plotted for each f_R scan, as labelled. In addition, the product of those numbers, which gives the overall factor by which the fractional change in the SOLPS-calculated n_t or T_{et} differs from the fractional change predicted by the modified 2PM, are plotted for each simulation as black asterisks. A value of unity for this asterisk means that SOLPS predicts an identical scaling with f_R to the modified 2PM. To be clear, the asterisks give the factors by which the coloured lines shown previously in figures 2c and 2d deviate from the solid black line at $f_R = 2$. The utility of this exercise is that now the *reasons* for these deviations are revealed by the factors that comprise them.

We notice from figure 3 that changes in the 2nd and 5th factors in (9) and (10) (due to changes in M_t and T_{it}/T_{et} respectively) are small for all of the f_R scans; these factors play little role in causing discrepancies from the modified 2PM scaling with f_R. Furthermore, for the high density case, changes in all of the other factors are small as well, so that the high density f_R scan conforms well to the modified 2PM scaling. In the few cases where the 4th factors in (9) and (10) (due to losses along a flux ring) do change significantly across the f_R scan, we found that those changes are dominated by changes in f_{momloss} rather than f_{pwrloss}. For these attached simulations, changes in f_{momloss} come

‡ This last assumption turns out to be important and will be assessed in detail later.

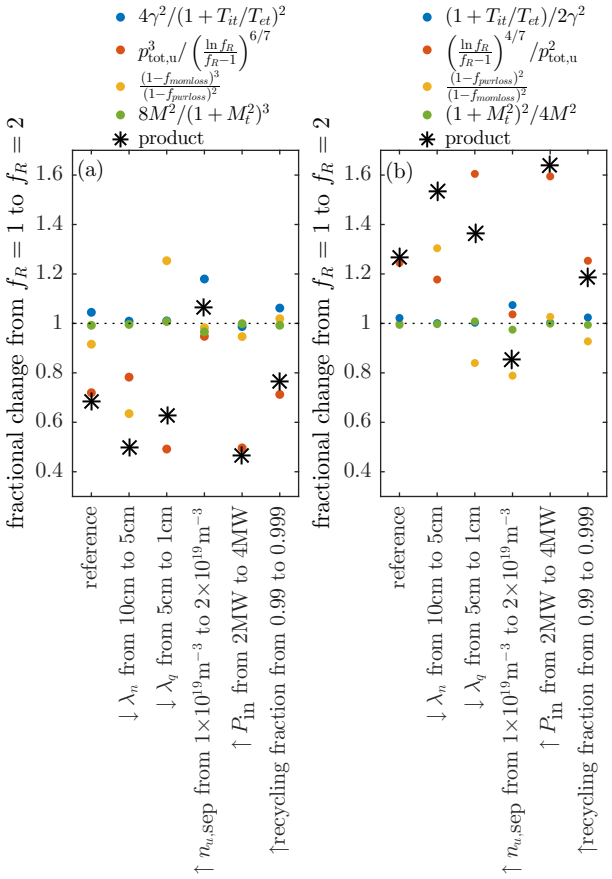

Figure 3. Fractional changes from $f_R = 1$ to $f_R = 2$ in the 2nd to 5th factors in equation (9) (figure a) and equation (10) (figure b), explaining discrepancies between the modified 2PM and the SOLPS simulations. See text for details. Colour version available online.

from changes in the parallel viscosity and in the radial divergence of momentum, not from changes in the momentum source due to neutrals. Overall, however, there is no general trend for the 4th factors.

Perhaps the most important thing to note from figure 3 is that for all of the f_R scans that produced a weaker scaling of n_t and T_{et} than the modified 2PM (i.e. all of the scans except the higher density scan – recall also figures 2c and 2d), the total upstream pressure decreased more strongly with f_R than expected from the modified 2PM; for these cases the red markers in figures 3a and 3b are less than and greater than one, respectively. This important result is now discussed further.

3.3. Understanding the stronger-than-expected decrease in upstream pressure with parallel area expansion

Since n_u was kept fixed for each scan and since the upstream dynamic pressure was always small compared to the upstream static pressure, a stronger-than-expected decrease in $p_{\mathrm{tot},u}$ amounts to a stronger-than-expected decrease in $T_{eu} + T_{iu}$. Now, consider the following equations for T_{eu} and T_{iu}, derived by integrating the electron and ion heat conduction equations along a field line whose major radius varies linearly in the parallel direction (Petrie *et al* 2013):

$$T_{eu} = \left(\frac{7\tilde{q}_{e\|u} L}{2\kappa_{0e}} \left[\frac{\ln f_R}{f_R - 1} \right] + T_{et}^{7/2} \right)^{2/7}, T_{iu} = \left(\frac{7\tilde{q}_{i\|u} L}{2\kappa_{0i}} \left[\frac{\ln f_R}{f_R - 1} \right] + T_{it}^{7/2} \right)^{2/7}, \tag{11}$$

where $\tilde{q}_{e\|u}$ and $\tilde{q}_{i\|u}$ are the electron and ion parallel internal energy flux densities upstream, $\kappa_{0e} = 2000$ and $\kappa_{0i} = 60$ are the electron and ion parallel conductivity coefficients, respectively (Stangeby *et al* 2000).

Equations (11) assume that conduction dominates both electron and ion parallel internal energy transport, that R varies linearly in the parallel direction (which is exactly met on the grids used here), and that there are no losses of electron or ion internal energy along the considered flux ring. Importantly, in order to achieve the modified 2PM scalings (5) and (6), it is also necessary to assume a sufficient drop in temperature along the flux ring so that the target temperature can be neglected (often referred to as the conduction-limited regime). This must be true *throughout the scan over* f_R. If, however, we are in a regime where at any point (or indeed all points) in the f_R scan the SOL is sheath-limited and the target temperature *cannot* be neglected, then the drop in upstream temperature (and therefore the upstream total pressure) will be larger than predicted by the modified 2PM. As a result, the third factors in (9) and (10) become less than and greater than one, respectively, so that n_t and T_{et} exhibit a weaker dependence on f_R§. The fact that n_t is more sensitive to $p_{\mathrm{tot},u}$ than T_{et} also explains why underestimating the decrease in $p_{\mathrm{tot},u}$ with f_R leads to larger discrepancies from the modified 2PM for n_t than for T_{et}, as seen in figures 2 and 3.

To demonstrate this effect, we concentrate on the high power f_R scan in which P_{in} was increased from the reference value of 2 MW to 4 MW. As already recognised, this scan exhibits the largest discrepancies in the fractional changes in n_t and T_{et} compared to the modified 2PM. However, the effect was observed to lesser extents in all of the f_R scans which displayed a more conservative scaling for n_t and T_{et} compared to the modified 2PM. Figure 4 plots equations (11) as a function of the SOLPS-calculated upstream temperature for the high power f_R scan, both excluding the target temperature terms (blue lines) and including them (red lines). The arrows point in the direction of increasing f_R.

§ It may seem counter-intuitive that the target electron temperature increases with decreasing upstream electron temperature for fixed upstream particle and electron energy flux density. Physically, this is due to a necessity to increase the target sound speed in order to maintain power balance when the upstream electron energy flux density remains the same but the upstream electron temperature decreases.

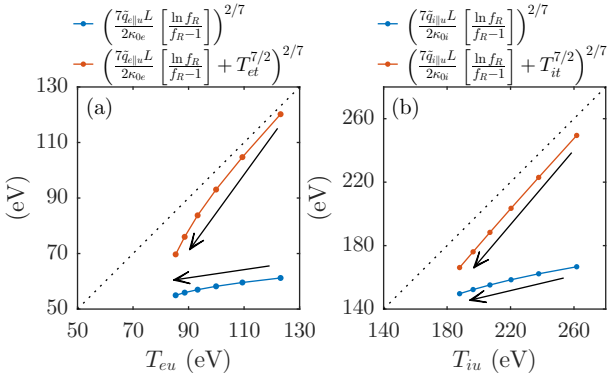

Figure 4. Comparison of equations (11) to the SOLPS-calculated upstream electron (a) and ion (b) temperatures for the high power f_R scan. Cases where the target temperature is included and excluded are shown, as labelled. Arrows point in the direction of increasing f_R. Colour version available online.

A good agreement is found between equations (11) and the simulated upstream temperatures when the target temperature is included, suggesting that parallel conduction dominates over convection in the simulation and that internal energy losses from both electrons and ions are small. Importantly, however, when the target temperature is excluded (as assumed in the 2PM), the predicted drop in upstream temperature is much less than was simulated. Note that the blue and red lines almost converge at high f_R, suggesting that including the target temperature becomes less important, i.e. the simulation moves from the sheath-limited to the conduction-limited regime, as the grid is rotated outwards.

3.4. Effect of parallel area expansion on the transition from sheath-limited to conduction-limited regimes

(Kotschenreuther *et al* 2010) extended the two-point analysis of (Stangeby 2000 – equation (4.110)) to find that, for a constant ratio of target to upstream temperatures, $n_u|_{T_{et}/T_{eu}} \propto \tilde{q}_{e\|u}^{4/7}/f_R L^{3/7}$. Under the assumption that R varies linearly in the parallel direction (i.e. rearranging the equations in the appendix of (Petrie *et al* 2013), we find a slightly modified version:

$$n_u|_{T_{et}/T_{eu}} \propto \frac{\tilde{q}_{e\|u}^{4/7}}{L^{3/7} f_R} \left(\frac{\ln f_R}{f_R - 1} \right)^{3/7}. \tag{12}$$

An upstream density scan, described in more detail in section 4, was carried out on the $f_R = 1$ and $f_R = 2$ grids. Figure 5 plots the resulting T_{et}/T_{eu} as a function of n_u. Defining (rather arbitrarily) the transition from sheath-limited to conduction-limited regimes to occur at $T_{et}/T_{eu} = 1/3$, we observe that the $f_R = 2$ case transitions at 0.53 times the density of the $f_R = 1$ case ($n_u = 1.12 \times 10^{19}$ m^{-3} compared to $n_u = 2.10 \times 10^{19}$ m^{-3}). This compares well to equation (12), which predicts a factor 0.58 difference. Note that at these low densities the recycling model had no effect on this result.

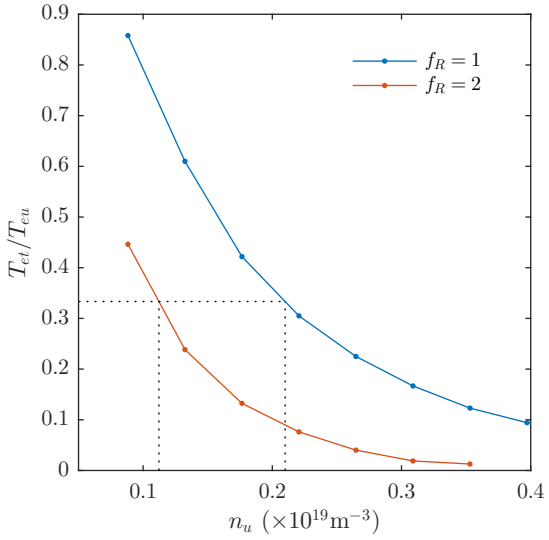

Figure 5. Transition from the sheath-limited to conduction-limited regimes as a function of n_u, for $f_R = 1$ and $f_R = 2$. The interpolated values of n_u at which $T_{et} = T_{eu}/3$ are also shown. Colour version available online.

4. Density-driven detachment onset; results and analysis

4.1. Rollover as a function of upstream density

In order to understand the effect of parallel area expansion on detachment onset, scans in the upstream separatrix density $n_{u,\mathrm{sep}}$ were performed on an $f_R = 1$ grid (representing a conventional slot divertor) and on an $f_R = 2$ grid (representing a Super-X divertor). To assess the sensitivity to the pumping model, the following four pumping models (i.e. combinations of F_{recyc} and F_{pump}) were tested on both grids: (i) $F_{\mathrm{recyc}} = 0.99$, $F_{\mathrm{pump}} = 0$, (ii) $F_{\mathrm{recyc}} = 0.999$, $F_{\mathrm{pump}} = 0$, (iii) $F_{\mathrm{recyc}} = 1$, $F_{\mathrm{pump}} = 0.01$, (iv) $F_{\mathrm{recyc}} = 1$, $F_{\mathrm{pump}} = 0.05$. All other input parameters were kept the same as for the reference case described in section 3.1. We discuss only detachment onset in pure deuterium plasmas driven by an increase in the upstream density; detachment via impurity seeding is left for future work.

Figure 6 shows n_t as a function of n_u. For all of the figures in this section, values were taken at the radial position where the target internal energy flux density ($\tilde{q}_{ixt} + \tilde{q}_{ext}$) was maximum for the lowest density cases (at $y = y_{\mathrm{sep}} + 1.6$ cm, corresponding to the third SOL ring). Plots are made for $f_R = 1$ (blue markers) and $f_R = 2$ (red markers) and for each pumping model (distinguished by different marker shapes, as labelled). We observe that, when n_t does roll over, it does so at approximately half the upstream density when the parallel area expansion is doubled ($n_u = 2.3 \times 10^{19}$ m^{-3} at rollover for $f_R = 2$ compared to $n_u = 4.5 \times 10^{19}$ m^{-3} at rollover for $f_R = 1$). Furthermore, the value of n_t at rollover for $f_R = 2$ is approximately half its value at rollover for $f_R = 1$ ($n_t = 8.5 \times 10^{20}$ m^{-3} at rollover for $f_R = 2$ compared to $n_t = 16.2 \times 10^{20}$ m^{-3} at rollover for $f_R = 1$).

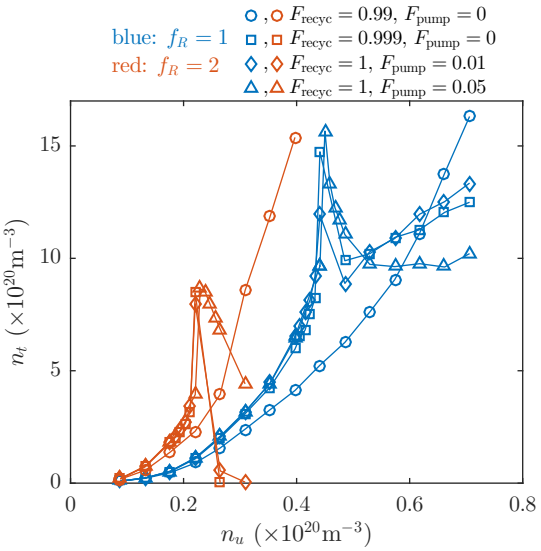

Figure 6. Target plasma density as a function of the upstream separatrix plasma density for the $f_R = 1$ (conventional) grid (blue) and the $f_R = 2$ (Super-X) grid (red), and for different pumping models (labelled with different marker shapes). Colour version available online.

As a side note, we also observe from figure 6 that the pumping model *can* influence the target plasma response to increasing upstream density. In particular, at high densities, the cases where pumping occurs entirely at the target via a recycling fraction $F_{\rm recyc} = 0.99$ (open circles) exhibit a different trend with n_u to the other pumping models. On the $f_R = 1$ grid there was no rollover in n_t for this pumping model, across the entire range of (physically reasonable) upstream densities investigated. On the $f_R = 2$ grid for $n_u > 4 \times 10^{19}$ m^{-3}, the target oscillated between attached and detached solutions (not shown in figure 6). Although an explanation of this behaviour is beyond the scope of this paper, we present it here because it is typically assumed that the pumping model does not affect the target plasma as long as the recycling flux is dominant (Chankin *et al* 2006). The reason why we do see an effect of the pumping model even though the recycling flux is dominant will be a topic of future work. We concentrate here on the three other pumping models which all exhibit a similar rollover behaviour as a function of upstream density.

4.2. Rollover as a function of target temperature

Figure 7a shows n_t as a function of T_{et} for the three pumping models which did exhibit a rollover on both grids. The markers denote steady-state simulations, while the solid lines show the time-dependent path taken by simulations in which the density was increased from an upstream density just before rollover to an upstream density just after rollover (for the $F_{\rm recyc} = 0.999$, $F_{\rm pump} = 0$ pumping model). This path is seen to be consistent with the steady state simulations and enabled us to capture more accurately the target

electron temperature at which n_t rolled over.

For both $f_R = 1$ and $f_R = 2$, the value of T_{et} at which the rollover occurred was very similar: $T_{et} = 0.59$ eV at rollover on the $f_R = 1$ grid and $T_{et} = 0.53$ eV at rollover on the $f_R = 2$ grid (note that we define target values at the interface between the last grid cell and the guard cell; at the centre of the last grid cell T_e was 0.73 eV at rollover on the $f_R = 1$ grid and 0.83 eV at rollover on the $f_R = 2$ grid). These temperatures are labelled with vertical dashed lines in figure 7. Given this, the fact that n_t rolls over at approximately half the value of n_u for twice the value of f_R is entirely consistent with the modified 2PM; equation (A13) in (Petrie *et al* 2013) predicts that $n_u \propto \frac{1}{\sqrt{T_{et}}} \frac{1}{f_R} \left[\frac{\ln f_R}{f_R - 1}\right]^{-2/7}$. Also, equation (A12) in (Petrie *et al* 2013) predicts that $n_t \propto \frac{1}{T_{et}^{3/2}} \frac{1}{f_R}$, in line with the value of n_t at rollover on the $f_R = 2$ grid being half the value of n_t at rollover on the $f_R = 1$ grid, given that the rollover occurs at the same target temperature.

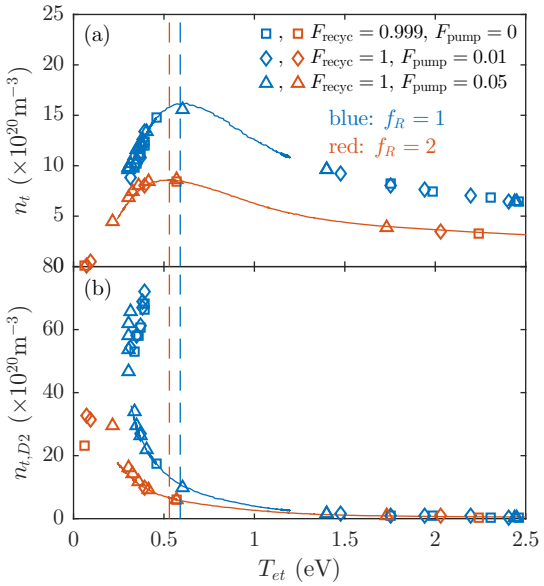

Figure 7. Target plasma density (a) and target molecular density (b) as functions of the target electron temperature during upstream-density-driven detachment. Colours and marker are the same as figure 6. Colour version available online.

We hypothesise that the target temperature at rollover is the same in both cases because this is the target temperature at which the the molecular density rises strongly (presumably due to a rapid decrease in the molecular dissociation rate) and elastic collisions with molecules are able to remove sufficient parallel momentum from the ions in order to induce a rollover. This hypothesis will be investigated further in a forthcoming paper. We note here that, as shown in figure 7b, a steep rise in the target molecular density was observed, beginning at the same value of T_{et} at which n_t rolled over. This is consistent with the important role of D_2 molecules previously reported by (Kotov and Reiter 2009).

5. Conclusions and future work

In this work, by operating SOLPS-5.0 in a minimally complex geometry, we have isolated and assessed the role of parallel area expansion (also known as total flux expansion) on the target plasma. Modelling only a single isolated slot divertor leg, we have demonstrated that at upstream densities for which the SOL remains in the attached, conduction-limited regime throughout the scan in f_R, the scalings of n_t and T_{et} with f_R predicted by SOLPS-5.0 (in the absence of currents, drifts and impurities) are well reproduced by the modified 2PM (Petrie *et al* 2013). If, however, the SOL is sheath-limited for any of the f_R scan, then the increase (decrease) in n_t (T_{et}) with f_R reported by SOLPS-5.0 is significantly weaker than predicted by the modified 2PM scaling.

This result is particularly important when considering, for a given tokamak plasma, how much you would need to increase the parallel area expansion in order to reach a given target temperature (at which, for example, you would expect the target to detach or the physical sputtering to reduce). If that given plasma is in the sheath limited regime, then the required increase in parallel area expansion would be more than predicted by the modified 2PM, and some other model (such as SOLPS-5.0) is required to predict how much more.

Upstream density scans were carried out on the $f_R = 1$ and $f_R = 2$ grids. The transition from sheath-limited to conduction-limited regimes was seen to occur at approximately half the upstream density on the $f_R = 2$ grid compared to the $f_R = 1$, in good agreement with the modified 2PM prediction (equation (12)).

As the upstream density was increased further, we found that the target plasma became sensitive to the particular pumping model used. In particular, simulations where pumping was implemented via a target recycling coefficient of 0.99 failed to roll over at densities up to twice those at which simulations with the other tested pumping models did roll over. The other three pumping models tested did detach at very similar upstream densities, however.

Importantly, the target electron density was found to roll over at almost the same target electron temperature on both $f_R = 1$ and $f_R = 2$ grids. Given this, the modified 2PM predicts that both the upstream plasma density required for rollover, as well as the target plasma density at which rollover occurs, should be halved when f_R is doubled. This is indeed what was observed in the simulations. We have hypothesised that the rollover in target density occurs at such similar target temperatures because of the sharp increase in molecular density that occurs at that temperature (presumably because of a decrease in the molecular dissociation rate), allowing molecular elastic scattering to remove ion parallel momentum and thereby induce rollover.

As well as testing the above hypothesis, future work will assess the role of impurities in density-driven detachment, as well as impurity-driven detachment. We will also assess the stability of the detachment front once it has pulled off from the target and investigate the detachment window of upstream density in which the detachment front remains below the X-point.

Appendix

Appendix A.1. Scaling of the total parallel energy flux density at the target with f_R

In the case that the integrated energy loss along each flux tube does not vary with parallel area expansion, we expect the total parallel energy flux density at the target to vary simply as

$$Q_{\|t} \propto \frac{1}{f_R}, \tag{A.1}$$

where $Q_{\|t} = \frac{5}{2} n u_{\|} T_e - \frac{1}{h_x b_x} \kappa_x^e \frac{\partial T_e}{\partial x} + \frac{5}{2} n u_x T_i - \frac{1}{h_x b_x} \kappa_x^i \frac{\partial T_i}{\partial x} + \frac{1}{2} m n u_{\|}^3$ is the *total* parallel energy flux density at the target.

Figure A1a shows the absolute value of $Q_{\|t}$ for all of the f_R scans described in section 3.1. Figure A1b shows the same data plotted as a fractional change from the $f_R = 1$ case. We observe that the simulations show an excellent agreement to the expected $Q_{\|t} \propto \frac{1}{f_R}$ (black line). The slight exception to this is the higher density case, for which $Q_{\|t}$ decreased somewhat faster with increasing f_R than expected. We attribute this to an increase in $S_{\mathrm{IE}}^{\mathrm{tot}}$ along the considered flux tube, from 0.38 in the $f_R = 1$ case to 0.57 in the $f_R = 2$ case. This in turn is primarily due to a factor three increase in the Dα radiation for the $f_R = 2$ case. Physically, as f_R is increased in the higher density f_R scan, the target electron temperature becomes sufficiently low that Dα radiation becomes significant, resulting in a slightly stronger scaling than $Q_{\|t} \propto \frac{1}{f_R}$.

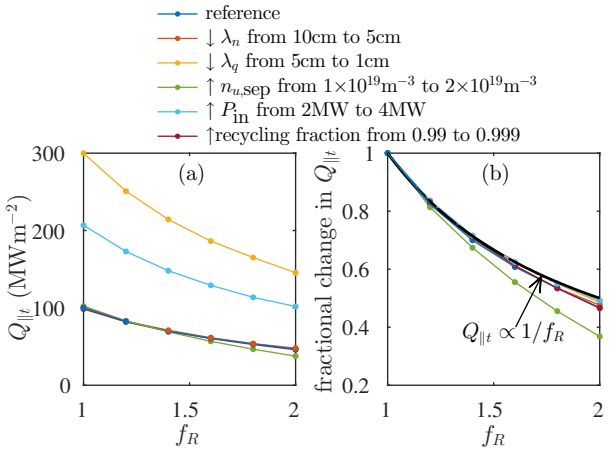

Figure A1. Simulated $Q_{\|t}$ as a function of f_R for the same simulation scans described in section 3.1. Values are plotted at the position of maximum target internal energy flux density. (a) shows absolute values while (b) shows the fractional changes relative to the $f_R = 1$ case, with the scaling $Q_{\|t} \propto \frac{1}{f_R}$ shown for comparison (black line). Colour version available online.

Appendix A.2. Definitions of $S^{\mathrm{tot}}_{\mathrm{mom}}$ and $S^{\mathrm{tot}}_{\mathrm{IE}}$

Rearranging the steady-state parallel momentum equation (2) and integrating from target to divertor entrance gives the following equation for total pressure balance:

$$p_{\mathrm{tot},u} - p_{\mathrm{tot},t} = \int_t^u S^{\mathrm{tot}}_{\mathrm{mom}} dl, \tag{A.2}$$

where

$$S^{\mathrm{tot}}_{\mathrm{mom}} = S^{\mathrm{neut}}_{\mathrm{mom}} + \frac{1}{\sqrt{g}}\frac{\partial}{\partial x}\left(\frac{\sqrt{g}}{h_x^2}\frac{4}{3}b_x\eta_\parallel^i\frac{\partial u_\parallel}{\partial x}\right) - \frac{1}{\sqrt{g}}\frac{\partial}{\partial y}\left(\frac{\sqrt{g}}{h_y}mnu_y u_\parallel - \frac{\sqrt{g}}{h_y^2}\eta_y^i\frac{\partial u_\parallel}{\partial y}\right) - \frac{mnu_\parallel^2}{\sqrt{g}}\frac{\partial}{\partial x}\left(dA_\parallel\right) \tag{A.3}$$

and $dA_\parallel = s^y b_x$ is the flux tube area normal to the magnetic field. Also, adding equations (3) and (4) in the steady-state and integrating gives the following equation for total internal energy flux balance:

$$s^y_u\left(\tilde{q}_{exu} + \tilde{q}_{ixu}\right) - s^y_t\left(\tilde{q}_{ext} + \tilde{q}_{ixt}\right) = \int_t^u S^{\mathrm{tot}}_{\mathrm{IE}} dV, \tag{A.4}$$

where

$$S^{\mathrm{tot}}_{\mathrm{IE}} = S^{\mathrm{neut}}_{\mathrm{eIE}} + S^{\mathrm{neut}}_{\mathrm{iIE}} - \frac{1}{\sqrt{g}}\frac{\partial}{\partial y}\left(\frac{\sqrt{g}}{h_y}\left(\tilde{q}_{ey} + \tilde{q}_{iy}\right)\right) - \frac{nT_e}{\sqrt{g}}\frac{\partial}{\partial x}\left(\frac{\sqrt{g}}{h_x}u_x\right) - \frac{nT_i}{\sqrt{g}}\frac{\partial}{\partial x}\left(\frac{\sqrt{g}}{h_x}u_x\right) - \frac{4}{3}b_x\eta_x^i\left(\frac{1}{h_x}\frac{\partial u_\parallel}{\partial x}\right)^2 - \eta_y^i\left(\frac{1}{h_y}\frac{\partial u_\parallel}{\partial y}\right)^2 \tag{A.5}$$

Rearranging (A.2) and (A.4) and using the boundary condition on internal energy flux density at the target then yields equations (7) and (8) (Stangeby *et al* 2015). This procedure is similar to the one described in (Kotov and Reiter 2009), except that here we balance total pressure p_{tot}, resulting in a geometric term $-\frac{mnu_\parallel^2}{\sqrt{g}}\frac{\partial}{\partial x}\left(dA_\parallel\right)$ in $S^{\mathrm{tot}}_{\mathrm{mom}}$, while (Kotov and Reiter 2009) balanced total *force* $b_x s^y p_{\mathrm{tot}}$, resulting in a geometric term $\frac{p}{\sqrt{g}}\frac{\partial}{\partial x}\left(dA_\parallel\right)$ in $S^{\mathrm{tot}}_{\mathrm{mom}}$. The latter term cannot be ignored in the force balance for a super-X divertor, while the former typically can. This is because p tends to be non-negligible along the entire SOL whereas $u_\parallel$ generally only rises over a small region close to the target. The other difference from (Kotov and Reiter 2009) is that we are balancing internal energy fluxes while they balanced total energy fluxes. This results in the third and fourth terms in (A.5) which were not present previously. In our simulations these terms do not typically play a significant role.

Acknowledgements

The authors would like to thank Peter Stangeby for some very useful discussions. This work has been carried out within the framework of the EUROfusion Consortium and has received funding from the Euratom research and training programme 2014-2018 under grant agreement No 633053 and from the RCUK Energy Programme (grant number EP/I501045). To obtain further information on the data and models underlying

this paper please contact PublicationsManager@ccfe.ac.uk. The views and opinions expressed herein do not necessarily reflect those of the European Commission.

References

Balescu R 1988 *Transport Processes in Plasmas*, Vol 1 (Amsterdam: North-Holland)
Chankin A V *et al* 2006 *Plasma Phys. Control. Fusion* **48** 839
Dekeyser W *et al* 2011 *B2-B2.5 Code Benchmarking* (available at www.eirene.de)
Fishpool G *et al* 2013 *J. Nucl. Mater.* **438** S356
Havlíčková E *et al* 2015 *Plasma Phys. Control. Fusion* **57** 115001
Kirk A *et al* 2004 *Plasma Phys. Control. Fusion* **46** 1591
Kotov V *et al* 2008 *Plasma Phys. Control. Fusion* **50** 105012
Kotov V and Reiter D 2009 *Plasma Phys. Control. Fusion* **51** 115002
Kotschenreuther M *et al* 2010 *Nucl. Fusion* **50** 035003
Lipschultz B *et al* 2016 *Nucl. Fusion* **56** 056007
Petrie T W *et al* 2013 *Nucl. Fusion* **53** 113024
Reiter D 2005 *The EIRENE Code User Manual* (available at www.eirene.de)
Sawada K and Fujimoto T 1995 *J. Appl. Phys.* **78** 2913
Schneider R *et al* 2006 *Contrib. Plasma Phys.* **46** 3
Stangeby P C 2000 *The Plasma Boundary of Magnetic Fusion Devices* (Bristol: IOP Publishing)
Stangeby P C *et al* 2015 *APS 2015* (available at http://starfire.utias.utoronto.ca/divimp/publications/Stangeby_APS_18N
Theiler C *et al* 2016 *submitted to Nucl. Fusion*
Thornton A J *et al* 2014 *Plasma Phys. Control. Fusion* **56** 055008
Umansky M V *et al* 2016 *J. Nucl. Mater. Energy* In press
Wischmeier M *et al* 2015 *J. Nucl. Mater.* **463** 22